

AERO-MECHANICAL ANALYSIS OF A BIRD-INSPIRED ORNITHOPTER USING AN INTEGRATED SIMULATION FRAMEWORK

Hyeon-Ho Yang[1], Sang-Gil Lee[1], Eun-Hyuck Lee[1], Hyeong-Seok Ko[1] & Jae-Hung Han[1]

[1]Korea Advanced Institute of Science and Technology, Daejeon, 34141, Republic of Korea

Abstract

This study presents an aero-mechanical analysis of a bird-inspired ornithopter using an integrated simulation framework, the ORNithopter Integrated Simulation Program (ORNISP). This framework combines a commercial multi-flexible-body dynamics solver (RecurDyn) with a modified Unsteady Vortex Lattice Method (UVLM) to capture the fluid-structure interaction during flapping flight. A forward-flight simulation environment for a single-joint ornithopter is constructed, incorporating linkage-driven wing kinematics and a flexible wing structure, and the model is validated against flight-test data from the hardware prototype KRoFalcon-S. Using this framework, the effects of the main spar stiffness and the mean dihedral angle on the longitudinal flight dynamics and the crank driving torque are investigated. The results indicate that the main spar must be stiff enough to generate sufficient aerodynamic force for sustained flight; beyond a moderate stiffness, however, the climb rate improves only marginally while the body pitch oscillations and the mean mechanical power continue to increase, so the lowest stiffness meeting the climb requirement is preferred. A positive mean dihedral angle improves the longitudinal stability and the forward-flight performance while slightly reducing the mean mechanical power over the range tested.

Keywords: Ornithopter, Fluid-Structure Interaction, Multi-Flexible-Body Dynamics, Integrated Simulation

1. Introduction

Bird-inspired ornithopters generate lift and thrust through periodic wing flapping, giving them maneuverability and efficiency at low flight speeds beyond those of conventional fixed-wing and rotary-wing aircraft [1, 2]. Most such vehicles use a single-joint main wing driven by a linkage mechanism, together with a tail for stability and control [3, 4]. Despite progress in flapping mechanisms [5], their development still depends largely on iterative hardware testing and empirical parameter tuning. This restricts a systematic exploration of the design space and makes it difficult to find configurations that balance aerodynamic performance, efficiency, and flight stability.

The principal difficulty in ornithopter design is the strongly coupled fluid-structure interaction that governs flapping flight. Large-amplitude wing motion generates highly unsteady aerodynamic loads that deform the flexible wing, and this deformation feeds back on the instantaneous force distribution, so that the aerodynamic and structural responses must be evaluated together [6, 7]. Bird-inspired ornithopters also operate at moderately low Reynolds numbers, where unsteady mechanisms such as the leading-edge vortex govern force generation [8, 9], and the aerodynamic loads have been shown to depend strongly on the multi-degree-of-freedom wing motion [10].

Coupling computational fluid dynamics with computational structural dynamics resolves these phenomena accurately [11, 12], but its cost limits simulations to a handful of flapping cycles, whereas establishing trim, evaluating dynamic stability, and performing parametric design studies require hundreds of cycles. Reduced-order and quasi-steady models are computationally efficient but cannot

https://doi.org/10.71945/icas2026_0777

represent the unsteady wake [13, 14, 15]. A gap therefore remains between methods that are accurate but too expensive and methods that are efficient but insufficiently accurate for the design of bird-inspired ornithopters.

The unsteady vortex lattice method (UVLM) provides an intermediate-fidelity alternative that resolves the unsteady wake at a fraction of the cost of computational fluid dynamics [16] and has been adapted to flapping wings through leading-edge-vortex and wake-shedding corrections [17]. On this basis, the integrated simulation framework ORNISP was developed, coupling a modified UVLM with a multi-flexible-body dynamics model and validated on a simple flapping wing and a single-joint ornithopter [18]. The framework builds on a line of multi-flexible-body ornithopter simulation [19, 20] that has supported flapping-wing trajectory optimization [21] and the design and flight testing of a single-joint ornithopter [4].

While the passive longitudinal stability of ornithopters has been studied [22], the way in which specific structural and kinematic design parameters shape the coupled aero-mechanical behavior in forward flight is still not well understood. This study applies the ORNISP framework to forward-flight simulations of a single-joint ornithopter to investigate how the main spar stiffness and the mean dihedral angle affect the longitudinal flight dynamics and the crank driving torque. By identifying the design trade-offs that govern the climbing capability, body-pitch oscillation, longitudinal stability, and power consumption, the study supports a systematic, parametric approach to the design of bird-inspired ornithopters.

2. Numerical Method

2.1 Aerodynamic Model

The flapping-wing aerodynamic loads are obtained from the UVLM, a method of intermediate fidelity between full computational fluid dynamics and quasi-steady models. The method treats the air as an inviscid, incompressible, and irrotational potential flow, so the velocity field follows from a scalar potential Φ governed by Laplace's equation:

$$\nabla^2 \Phi = 0. \tag{1}$$

Each lifting surface is built from quadrilateral vortex-ring elements [16], and impermeability is imposed on the wing surface,

$$(\nabla \Phi + \mathbf{v}) \cdot \mathbf{n} = 0, \tag{2}$$

where $\mathbf{v}$ is the surface velocity produced by the wing motion and $\mathbf{n}$ the surface normal. Both evolve through the flapping stroke, and this time dependence is what makes equation (2) unsteady.

Each lifting surface is divided into $M \times N$ quadrilateral panels (Figure 1), every panel carrying a bound vortex ring of circulation Γ_{ij}, and the boundary condition is collocated at the panel centers. At each

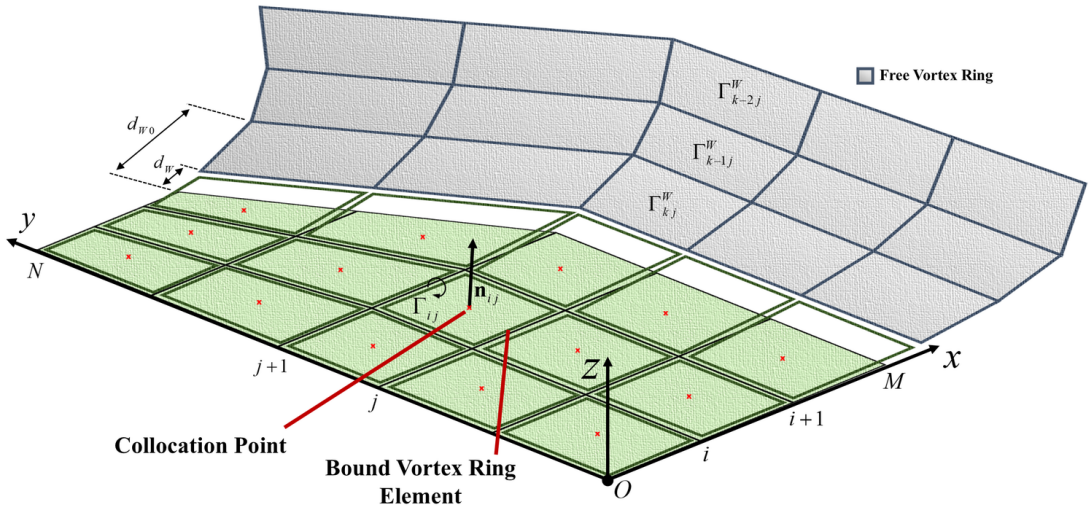


Figure 1 – Discretization of a lifting surface into $M \times N$ bound vortex-ring panels with collocation points, and the free vortex rings shed into the wake.

step the wake-shedding edge, usually the trailing edge, releases a free ring that carries the bound circulation held one step earlier. This carry-over conserves total vorticity in the sense of Kelvin's theorem as the solution marches in time. A shed ring is placed at a distance

$$d_W = \frac{d_{w0}}{\kappa}, \tag{3}$$

behind its shedding edge, where d_{w0} is the spacing to the most recently shed ring. The wake-shedding follows Ansari et al. [23], and the value $\kappa = 5$, proposed by Yang et al. [18], brings the resulting shed-ring spacing close to that recommended by Katz and Plotkin [16]. Collocating equation (2) over all $m = M \times N$ panels gives a linear system for the bound circulations,

$$\sum_{L=1}^{m} a_{KL}\,\Gamma_L = \mathrm{RHS}_K, \quad K = 1, \ldots, m, \tag{4}$$

where a_{KL} is the aerodynamic influence coefficient and the right-hand side gathers the kinematic and wake-induced normal velocities. The bound circulations then determine the panel pressure difference through the unsteady Bernoulli equation [16],

$$\Delta p_L(t) = \rho \left[\left\{ (U + u_W,\, V + v_W,\, W + w_W)_L \times \boldsymbol{\gamma}_L \right\} \cdot \mathbf{n}_L + \frac{1}{\Delta t} \left(\Gamma_L(t) - \Gamma_L(t - \Delta t) \right) \right], \tag{5}$$

where ρ is the air density, $\boldsymbol{\gamma}_L$ the panel vorticity vector (distinct from the scalar bound circulation Γ_L), $(U,V,W)_L$ the kinematic velocity, and $(u_W, v_W, w_W)_L$ the wake-induced velocity. Of the two bracketed terms, the first gives the steady contribution and the second accounts for the changing circulation. The load on each panel is

$$\mathbf{F}_L = \Delta p_L \Delta S_L \mathbf{n}_L, \tag{6}$$

where ΔS_L is the panel area; summing these elemental loads over all panels gives the resultant force and moment.

For bird-scale flapping flight, three additional schemes extend the conventional UVLM; their full formulation is given by Yang et al. [18]. To regularize the induced velocity where roll-up brings wake filaments close together, a growing vortex core [24] is introduced; its radius expands with the wake age t_W,

$$r_C(t_W) = \sqrt{r_{C0}^2 + 4\alpha_L \nu \left(1 + \frac{a_1 \Gamma}{\nu} \right) t_W}, \tag{7}$$

where r_{C0} is the initial core radius, $\alpha_L = 1.25643$ the Lamb constant, ν the kinematic viscosity, a_1 the Squire parameter, and Γ the circulation of the vortex filament; the finite core regularizes the Biot–Savart kernel that evaluates the induced velocities. The leading-edge vortex is represented by a Pseudo-Leading-Edge Vortex (PLEV) model, which avoids the instability of explicit leading-edge shedding by adding a vortex ring on the leading-edge panel with strength

$$\Gamma_P(t) = K_P(\alpha_{\mathrm{LE}})\,\Gamma_{\mathrm{LE}}(t), \tag{8}$$

in which K_P depends on the local angle of attack α_{LE} at the leading-edge panel and switches between lift enhancement and stall-like reduction. The spanwise flow of flapping flight is handled by an Adaptive Wake-Shedding (AWS) scheme, which sets the shed wake strength as

$$\Gamma^W(t) = K_W(\mathbf{v}_{\mathrm{WSE}})\,\Gamma_{\mathrm{WSE0}}(t), \tag{9}$$

where Γ_{WSE0} is the bound circulation of the wake-shedding panel and the coefficient K_W decays from unity toward zero as the local induced velocity $\mathbf{v}_{\mathrm{WSE}}$ rotates off the shedding-edge direction; the split of Γ_{WSE0} between the retained bound ring and the shed ring keeps the Kelvin condition satisfied.

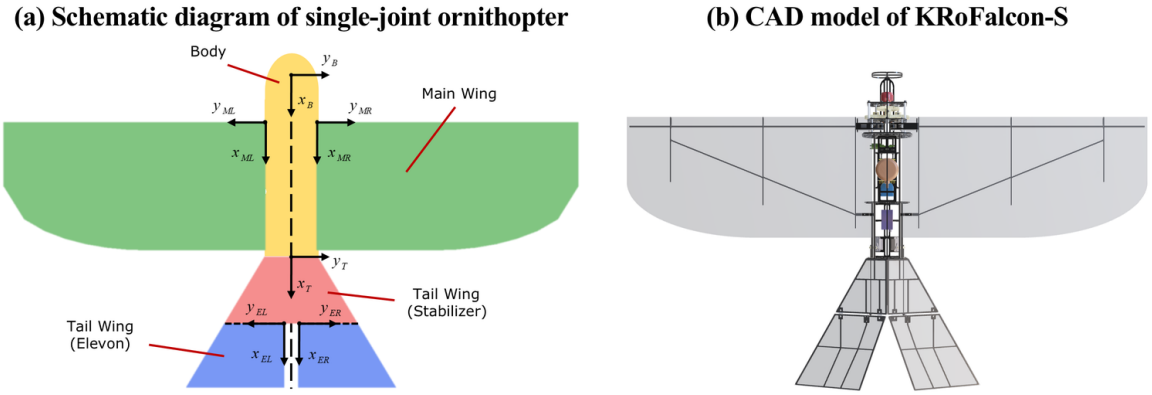


Figure 2 – (a) Schematic diagram of the single-joint ornithopter model and (b) CAD model of KRoFalcon-S.

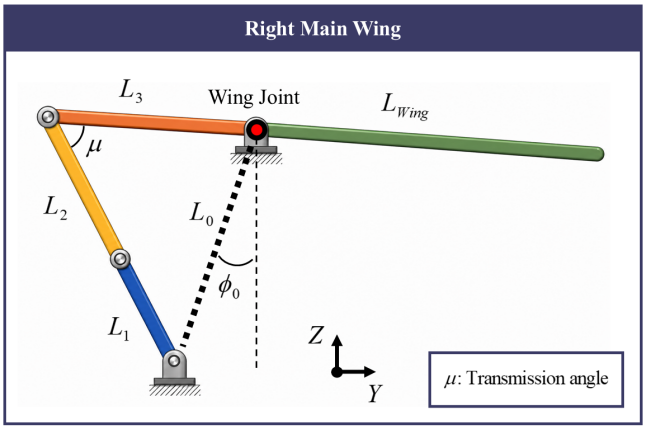


Figure 3 – Planar crank-rocker mechanism that drives the flapping motion of the inner wing, with the fixed link L_0, crank L_1, coupler L_2, rocker L_3, fixed-link angle ϕ_0, and transmission angle μ.

2.2 Ornithopter Simulation Model

The reference vehicle is KRoFalcon-S (KAIST Robotic Falcon with Simple wing), a single-joint ornithopter whose simulation model is shown in Figure 2. The model comprises one body, two flexible main wings, one tail wing, and two elevons, all of which except the body are treated as thin lifting surfaces. Each main wing is connected to the body by a revolute joint that permits flapping about the longitudinal axis, the tail is fixed to the body, and each elevon rotates about its hinge line for longitudinal control. Its deflection is denoted by the elevon angle θ_e, defined positive for a downward deflection, so that a negative θ_e raises the elevon and produces a nose-up pitching moment. The model is built from four rigid and two flexible bodies. The complete vehicle weighs 620 gf with a wingspan of about 1.1 m, and its moments of inertia, obtained from the CAD model, are $I_{xx} = 5.6 \times 10^{-3}$, $I_{yy} = 11.8 \times 10^{-3}$, and $I_{zz} = 16.5 \times 10^{-3}$ kg·m^2.

2.2.1 Kinematic model

The flapping motion of each main wing is generated by a planar crank-rocker mechanism (Figure 3), whose position is solved by the planar vector method [25]. The four links are the fixed link L_0, the crank L_1, the coupler L_2, and the rocker L_3, with the inner wing rigidly attached to the rocker so that the wing flapping angle follows the rocker angle. For a given crank angle θ_1, the closed-loop condition of the four-bar linkage,

$$\mathbf{d}_1 + \mathbf{r}_2 + \mathbf{r}_3 = \mathbf{0}, \tag{10}$$

where $\mathbf{d}_1$ is the diagonal from the crank to the rocker pivot and $\mathbf{r}_2$, $\mathbf{r}_3$ are the coupler and rocker vectors, is solved analytically for the coupler and rocker orientations. The force transmission of the

Table 1 – Optimized crank-rocker link parameters of the reference mechanism.

Parameter	Symbol	Value
Fixed-link angle	ϕ_0	12.0°
Fixed link	L_0	37.6 mm
Crank	L_1	10.0 mm
Coupler	L_2	33.5 mm
Rocker	L_3	20.0 mm
Flapping amplitude	A	60°
Mean dihedral angle	ψ_d	15°

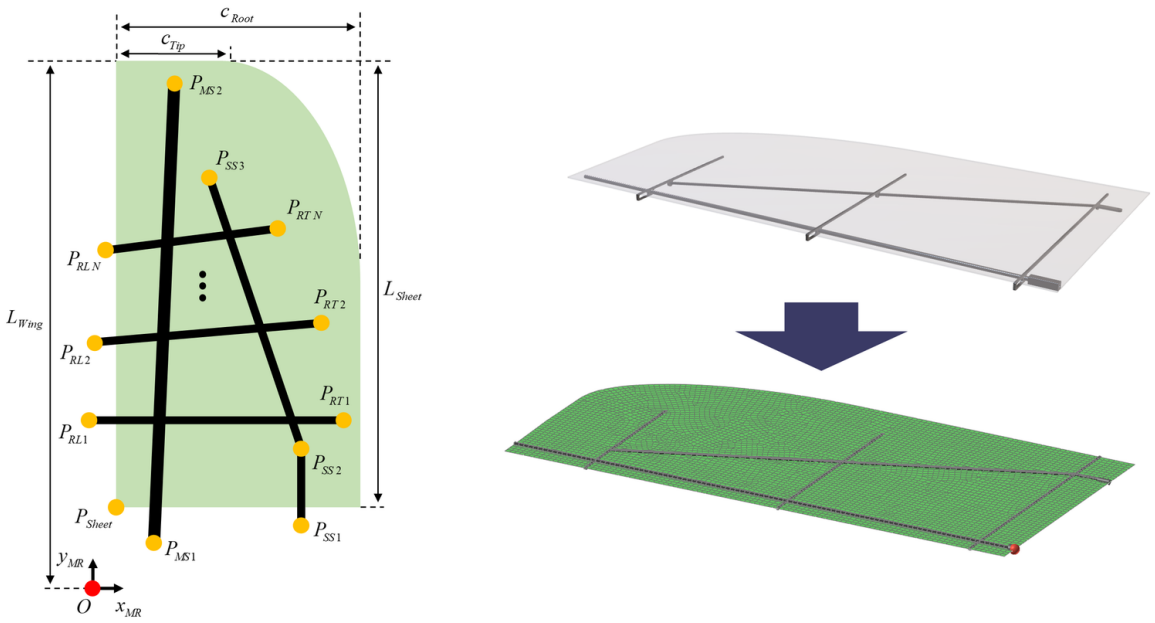


Figure 4 – Reference wing: (a) the main wing design parameters, with the spar, rib, and sheet reference points and the chord and span dimensions in the wing-fixed frame; (b) the CAD model of the wing structure (top) and the corresponding Full-Flex finite-element model (bottom), using beam elements for the main spar, sub-spar, and ribs and shell elements for the wing sheet.

linkage is measured by the transmission angle between the coupler and the rocker,

$$\mu = \arccos\left(\frac{L_2^2 + L_3^2 - |\mathbf{d}_1|^2}{2\,L_2\,L_3}\right), \tag{11}$$

held within $35^\circ \leq \mu \leq 145^\circ$ to avoid near-collinear configurations where transmission degrades [26]. The wing flapping amplitude is the peak-to-peak excursion of the inner wing angle over one crank revolution, and the mean dihedral angle ψ_d is the midpoint of that excursion. The link lengths follow from a genetic-algorithm optimization that targets a flapping amplitude of 60° and a mean dihedral angle of 15° while keeping the mean transmission angle near 90°; the resulting parameters are listed in Table 1.

2.2.2 Structural model

The main wing structure consists of a CFRP main spar, a CFRP sub-spar, three ribs, and an EPP wing sheet (Figure 4). Running along the leading edge, the main spar takes most of the bending and torsion; the sub-spar stiffens the section chordwise; and the ribs control how the wing sheet deforms. The wing frame is modeled with beam elements and the wing sheet with shell elements, merged at their coincident nodes into a Full-Flex (FFlex) finite-element model in RecurDyn so that the

Table 2 – Geometric and material parameters of the reference wing (Case B baseline).

Component	Parameter	Symbol	Value
Geometry			
Main spar	Outer diameter	$d_{\text{MS-out}}$	4.0 mm
	Inner diameter	$d_{\text{MS-in}}$	2.0 mm
	Cross-section	–	Hollow circle
Sub-spar	Width × height	$w \times h$	2.6×2.0 mm
Rib ($\times 3$)	Width × height	$w \times h$	2.0×2.0 mm
Wing sheet	Thickness	t	2.0 mm
	Root chord	c_{Root}	260 mm
	Tip chord	c_{Tip}	140 mm
	Sheet length	L_{Sheet}	520 mm
Material			
CFRP (frame)	Young's modulus	E_{CFRP}	86.4 GPa
	Density	ρ_{CFRP}	1513.3 kg/m^3
EPP (sheet)	Young's modulus	E_{EPP}	8 MPa
	Density	ρ_{EPP}	30 kg/m^3

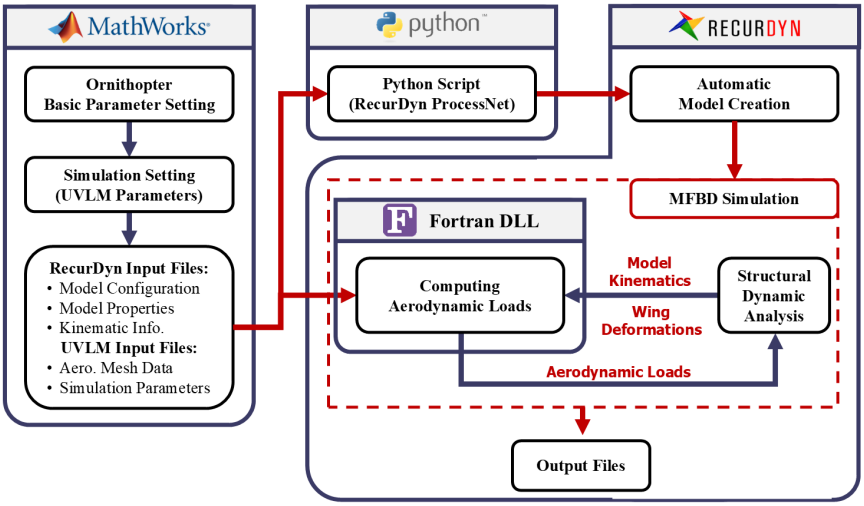


Figure 5 – Configuration of the integrated simulation framework: ORNISP.

passive wing pitching induced by the chordwise flexibility is reproduced. The geometric and material parameters of the reference wing are summarized in Table 2, and the reference wing structure used in the simulations is shown in Figure 4(b). The CFRP stiffness comes from in-house tests on CFRP tubing, while the EPP modulus follows Morton et al. [27]; both choices match those used on flight-proven ornithopters [18, 28].

2.3 Integrated Simulation Framework

The aerodynamic and structural models are coupled within the ORNISP framework shown in Figure 5. Coupling markers placed at the UVLM nodes and collocation points are each tied to the closest structural node, so that the lifting surface deforms with the structure and the panel loads return to the structural mesh. The coupled rigid-flexible system is integrated in RecurDyn [29], whose recursive solver combines a co-rotational finite-element formulation with generalized-α time stepping [30] and Newton–Raphson equilibrium iterations. Because the accumulated wake history makes each aerodynamic evaluation expensive, the loads are held fixed during the inner equilibrium iterations and recomputed only once a step has converged. The modified UVLM is implemented as a Fortran

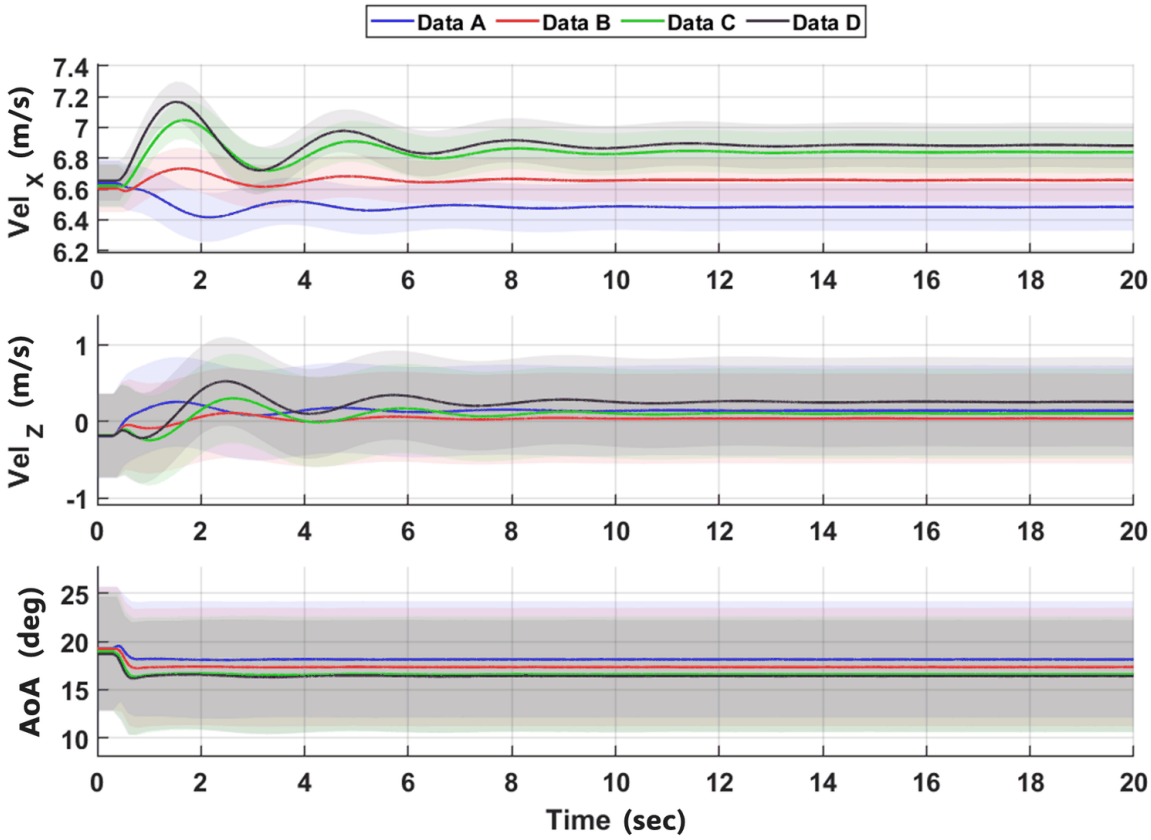


Figure 6 – Convergence of the longitudinal states to the forward-flight trim condition after the longitudinal degrees of freedom are released, shown for all four flight-test conditions (Data A–D).

dynamic-link library that RecurDyn calls as a user force routine, while a MATLAB application and a Python–RecurDyn interface automate the model generation, simulation, and post-processing that the parametric studies of section 3 require.

2.4 Validation

The framework is validated against forward-flight test data from the KRoFalcon-S hardware prototype, which carries a Pixhawk flight-control computer that estimates the flight speed and attitude from its inertial and GPS measurements. Four trim conditions were identified from the flight tests, with flapping frequencies of 6.7–7.1 Hz and flight speeds of 6.45–6.66 m/s. Each condition is reproduced in simulation by prescribing the measured flapping frequency and elevon angle, enforcing the wing kinematics over the first two flapping cycles, and then releasing the longitudinal degrees of freedom so that the model settles into its own trim state, as shown in Figure 6. The simulated trim values are taken as the average of the converged longitudinal states over the final four seconds of each run. The simulated and measured trim conditions are compared in Table 3: the flight speed is predicted within 3.8% and the body angle of attack within 7.8%. Each 20-second simulation, spanning more than 130 flapping cycles, takes about seven hours of wall-clock time on a sixteen-core processor, far below the cost of coupled computational-fluid-dynamics and computational-structural-dynamics analysis.

3. Aero-Mechanical Analysis

The integrated framework is applied to examine how the main spar stiffness and the mean dihedral angle govern the longitudinal flight dynamics of the single-joint ornithopter in forward flight.

3.1 Flight Simulation Conditions

The longitudinal flight simulations are performed under a laterally constrained condition with the elevon held fixed in each run, so that the inherent longitudinal dynamics are isolated from the lateral and control responses (Figure 7). Each simulation runs for 30 seconds. The vehicle starts from

Table 3 – Comparison of the simulated and flight-test trim conditions for the four flight-test data sets.

	Inputs		Flight speed (m/s)			Body AoA (deg)		
Data	f (Hz)	θ_e (deg)	Sim	Test	Err	Sim	Test	Err
A	7.1	-20.2	6.48	6.63	2.2%	18.1	18.7	3.0%
B	6.7	-18.4	6.66	6.45	3.2%	17.4	16.1	7.8%
C	6.7	-17.3	6.84	6.66	2.7%	16.6	15.8	5.0%
D	7.0	-17.5	6.88	6.63	3.8%	16.4	17.1	3.9%

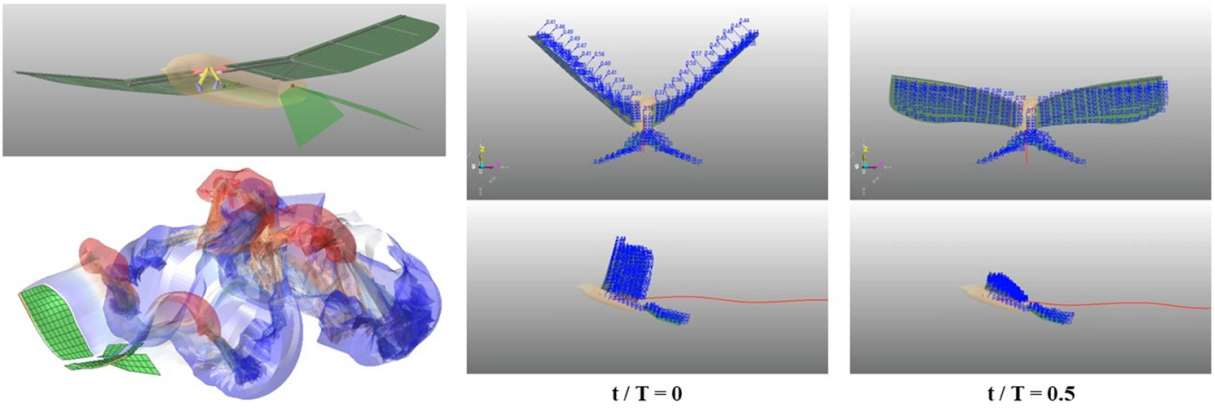


Figure 7 – Flight dynamic simulation of the single-joint ornithopter: the integrated model with its shed wake (left) and the wing kinematics together with the wake at two instants of the flapping cycle, $t/T = 0$ and $t/T = 0.5$ (right).

an initial flight speed of 6.5 m/s and a body pitch angle of 16°; the wing kinematics are enforced over the first two flapping cycles, after which the longitudinal degrees of freedom are released so that the vehicle settles into its own trim state. These degrees of freedom must be released because constraining the heaving and pitching motion would overestimate the lift and produce a spurious net thrust that does not represent free flight.

The energy cost of each configuration is characterized by the crank driving torque and the corresponding mechanical input power. Since the crank completes one revolution per flapping cycle, the instantaneous mechanical power follows from the crank torque as

$$P(t) = \max(0,\, \tau_{\text{crank}}(t)) \cdot 2\pi f, \tag{12}$$

where $f = 6.8$ Hz is the flapping frequency; the clipping to non-negative values excludes the motor-side regenerative phases, which a direct-drive motor does not recover. For the present configurations the crank torque stays non-negative over the cycle (Figure 10), so the cycle-averaged power reduces to $P_{\text{mean}} = 2\pi f\, \tau_{\text{mean}}$. The torque is reported in kg·cm throughout and converted to N·m in the power calculation, with 1 kg·cm corresponding to 0.0981 N·m. The mean mechanical power P_{mean} is reported alongside the torque for each configuration.

3.2 Effect of Main Spar Stiffness

Three wing configurations are compared, with main spar outer diameters of 3.0 mm (Case A), 4.0 mm (Case B), and 5.0 mm (Case C). In every case the inner diameter is 2.0 mm smaller than the outer, so the radial wall thickness is fixed at 1.0 mm and only the spar diameter varies; all other parameters are held at the reference values. To separate the structural effect from the longitudinal control input, each configuration is simulated at three elevon angles, $\theta_e = -5^\circ$, -15°, and -25°. The resulting flight trajectories and longitudinal states are presented in Figures 8 and 9, and the trim states and crank torques at the reference elevon angle of $\theta_e = -15^\circ$ are summarized in Table 4.

Figure 8 shows that the two inputs act on different motions: the elevon angle governs the forward distance, while the main spar stiffness governs the altitude. A smaller elevon deflection ($\theta_e = -5^\circ$)

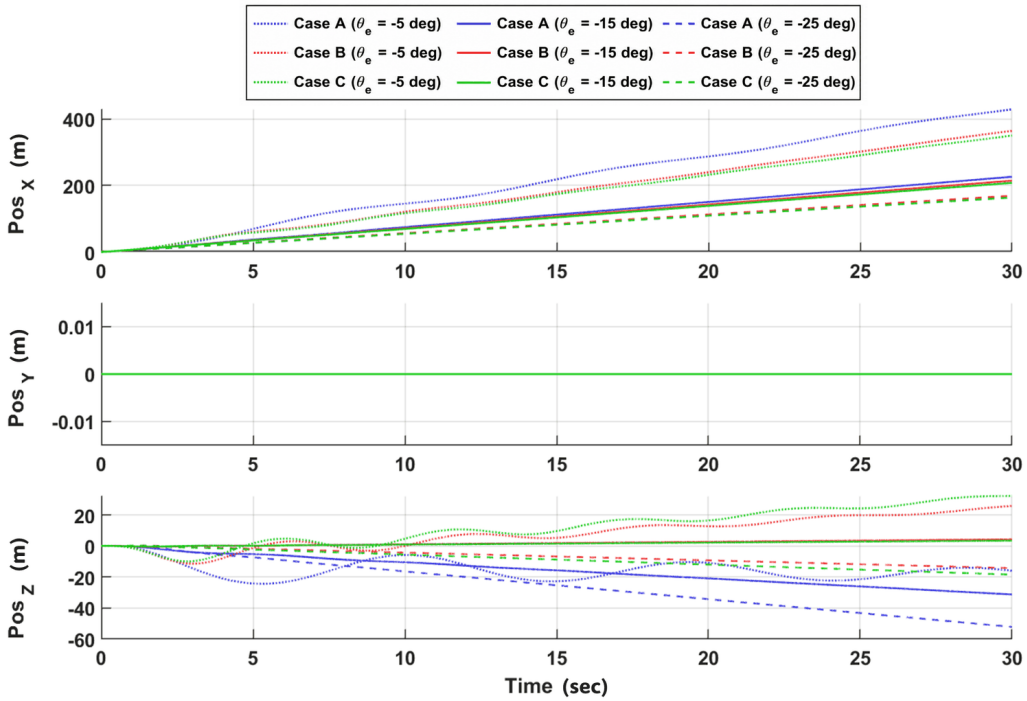


Figure 8 – Flight trajectories (X, Y, and Z positions) of the three main spar stiffness configurations (Case A, B, and C) at the elevon angles $\theta_e = -5°$, $-15°$, and $-25°$.

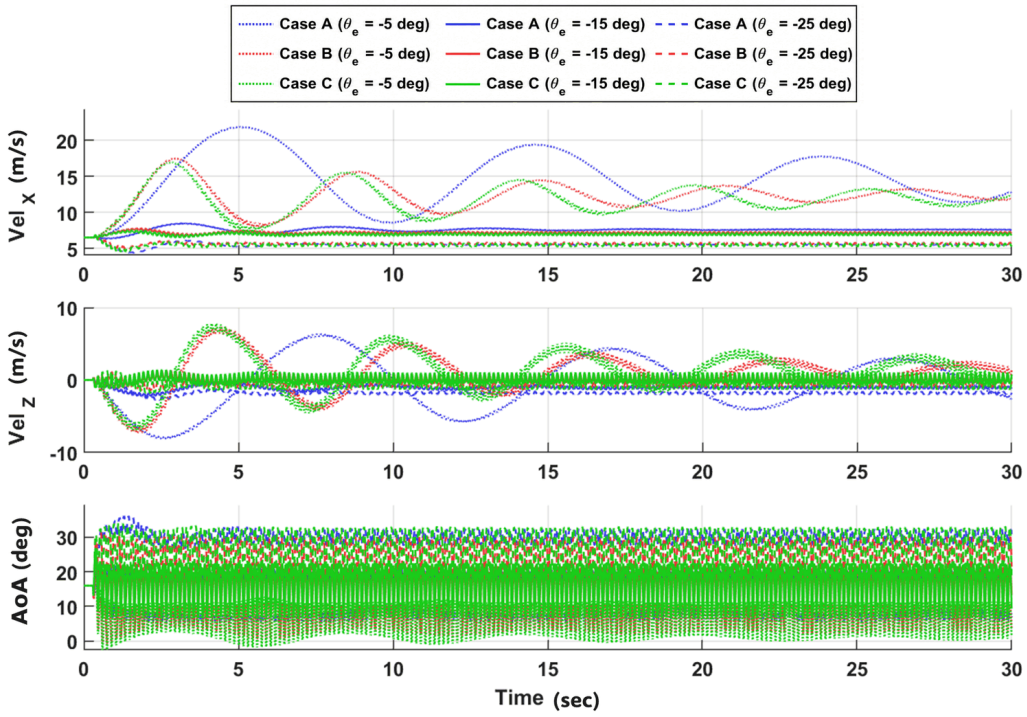


Figure 9 – Longitudinal velocity components and angle of attack of the three main spar stiffness configurations at the elevon angles $\theta_e = -5°$, $-15°$, and $-25°$.

produces the longest forward travel, whereas the climb is decided by the structure. The most flexible configuration, Case A, fails to gain altitude at any elevon setting and descends throughout, since its excessive deformation reduces the effective lift; at $\theta_e = -15°$ it ends 31.3 m below the launch altitude. The stiffer Case B and Case C instead climb at the smaller elevon deflections.

The longitudinal velocity and angle-of-attack histories in Figure 9 show how the structural flexibility shapes the unsteady response. The amplitude of the velocity and angle-of-attack oscillations grows

Table 4 – Trim states, crank driving torque, and mechanical power for the three main spar stiffness configurations at $\theta_e = -15^\circ$.

Case	d_{MS} (mm)	X (m)	Z (m)	V_x (m/s)	V_z (m/s)	AoA (deg)	τ_{mean} (kg·cm)	$\tau_{\max}$ (kg·cm)	P_{mean} (W)
A	3.0	226.5	-31.3	7.6	-1.0	18.4	6.3	24.0	26.4
B	4.0	214.8	4.2	7.2	0.2	15.3	16.1	43.7	67.4
C	5.0	208.2	3.4	7.0	0.3	15.0	19.4	50.3	81.3

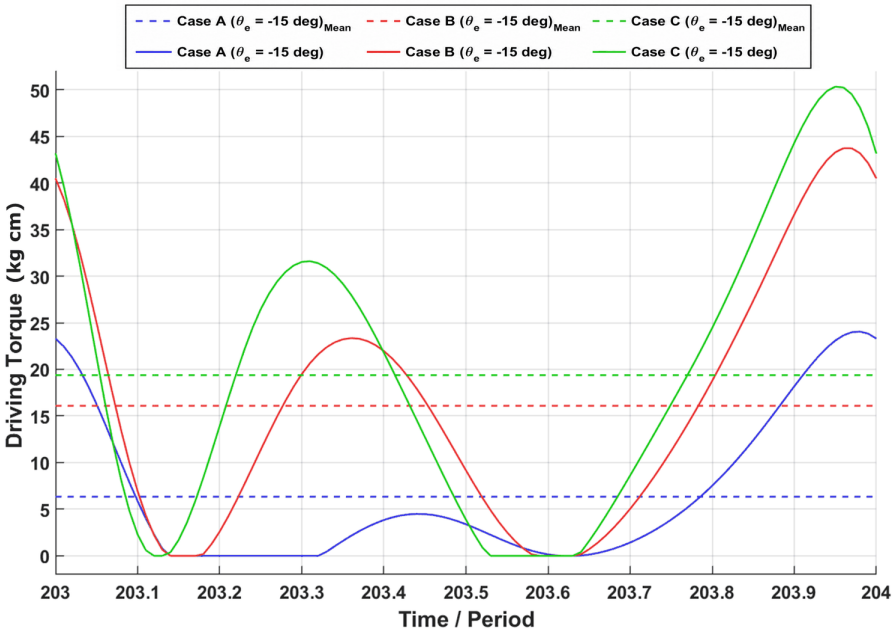


Figure 10 – Crank driving torque over one steady-state flapping cycle for the three main spar stiffness configurations at $\theta_e = -15^\circ$; the dashed lines denote the cycle-averaged values.

with the spar stiffness, consistent with a stiffer structure transmitting the unsteady aerodynamic loads to the body more directly while the flexible structure of Case A absorbs them. The trim states reached at $\theta_e = -15^\circ$ are listed in Table 4.

The crank driving torque over one steady-state flapping cycle is shown in Figure 10. The mean torque rises steeply with the spar stiffness, from 6.3 kg·cm for Case A to 16.1 and 19.4 kg·cm for Case B and Case C, corresponding to a mean mechanical power of 26.4, 67.4, and 81.3 W. Case A draws the least power but cannot sustain flight. Between the two flying configurations, Case C consumes about 20% more power than Case B but raises the steady climb rate by only 0.1 m/s (the trim V_z rises from 0.2 to 0.3 m/s). Increasing the spar stiffness beyond Case B therefore adds mean mechanical power and pitch oscillation for only a marginal gain in climb rate, a case of diminishing returns over the tested range. The lowest spar stiffness that still meets the climb requirement is thus the preferred design choice, with a stiffer spar reserved for missions that prioritize rapid altitude gain.

3.3 Effect of Mean Dihedral Angle

Three mean dihedral angles, $\psi_d = -15^\circ$, 0°, and $+15^\circ$, are evaluated for the Case B wing structure at the reference elevon angle of $\theta_e = -15^\circ$. The flight trajectories and longitudinal states are presented in Figures 11 and 12, and the trim states are listed in Table 5.

As shown in Figure 11, the negative dihedral configuration never settles, swinging through large altitude excursions that reach below -40 m before ending near -30 m, whereas the flat and positive dihedral configurations follow smooth, climbing trajectories. The positive dihedral angle reaches the best performance, with the longest forward distance of 214.8 m and an altitude gain of 4.2 m.

The velocity and angle-of-attack histories in Figure 12 show that the negative dihedral configuration sustains large-amplitude, long-period oscillations of a phugoid-like character and never reaches a steady trim, which is why its trim velocity and angle of attack are omitted from Table 5. The flat

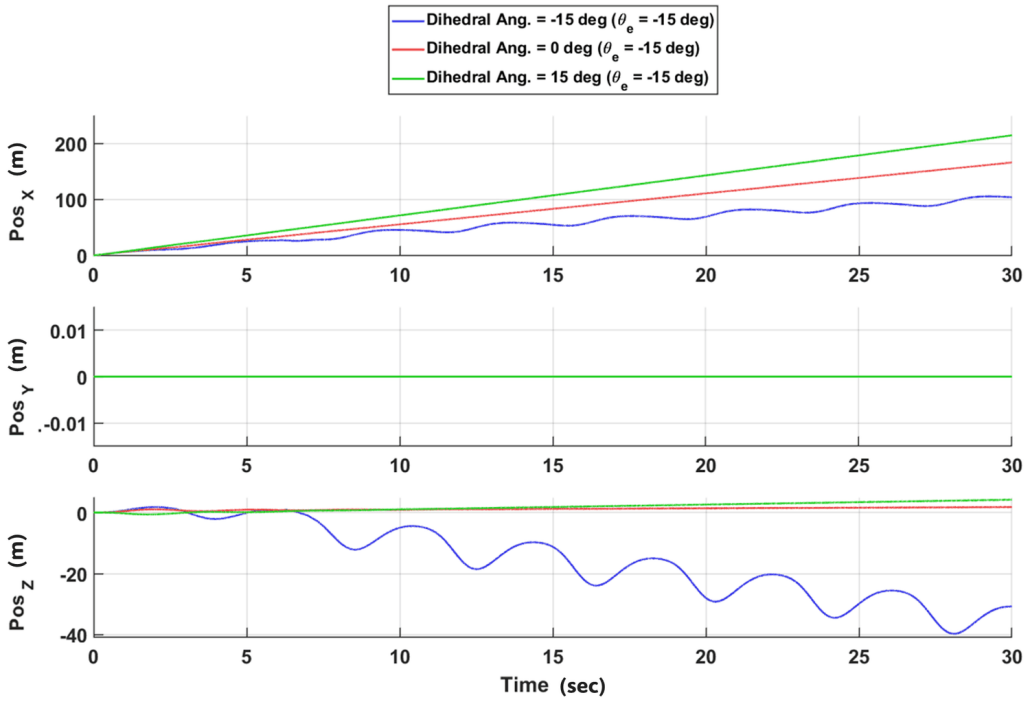


Figure 11 – Flight trajectories (X, Y, and Z positions) for the three mean dihedral angle configurations ($\psi_d = -15°$, $0°$, and $+15°$) of the Case B wing at $\theta_e = -15°$.

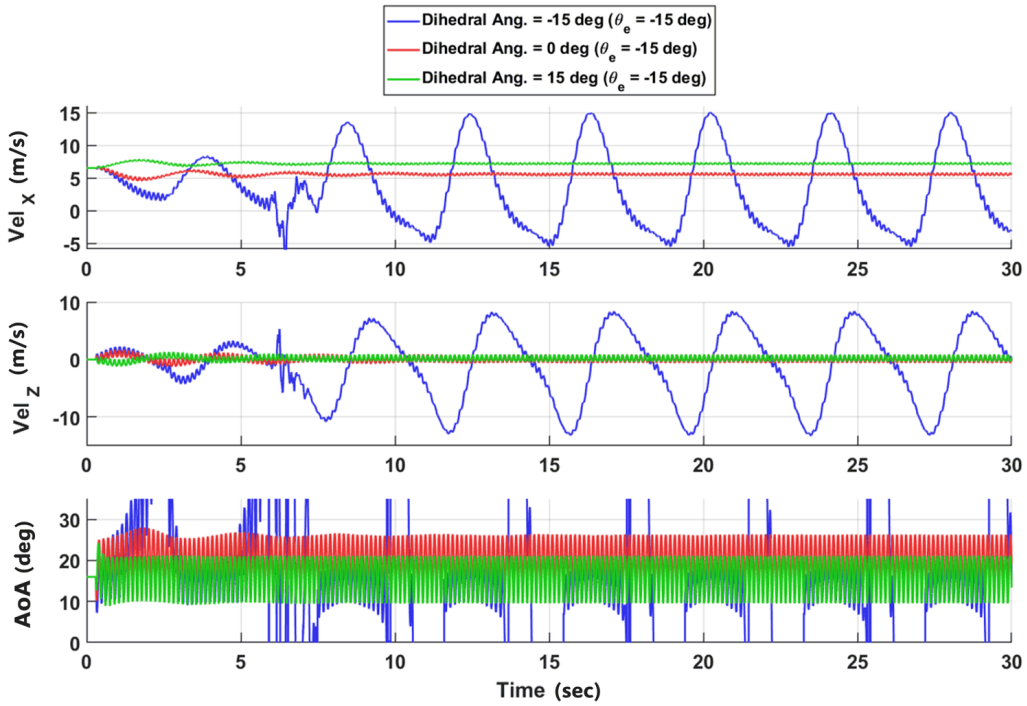


Figure 12 – Longitudinal velocity components and angle of attack for the three mean dihedral angle configurations of the Case B wing at $\theta_e = -15°$.

configuration ($\psi_d = 0°$) remains stable but settles at a relatively high trim angle of attack of $18.5°$ and a modest forward speed of 5.6 m/s. Increasing the dihedral to $+15°$ lowers the trim angle of attack to $15.3°$ and raises the forward speed to 7.2 m/s.

The crank driving torque in Figure 13 is almost insensitive to the mean dihedral angle: the mean mechanical power stays within 67.4 to 71.6 W across the three configurations and even decreases slightly as the dihedral increases from $-15°$ to $+15°$. Over the range tested, a positive mean dihe-

Table 5 – Trim states, crank driving torque, and mechanical power for the three mean dihedral angles (Case B, $\theta_e = -15°$).

ψ_d (deg)	X (m)	Z (m)	V_x (m/s)	V_z (m/s)	AoA (deg)	τ_{mean} (kg·cm)	P_{mean} (W)
-15	104.0	-30.0	–	–	–	17.1	71.6
0	166.2	1.8	5.6	0.1	18.5	17.0	71.2
$+15$	214.8	4.2	7.2	0.2	15.3	16.1	67.4

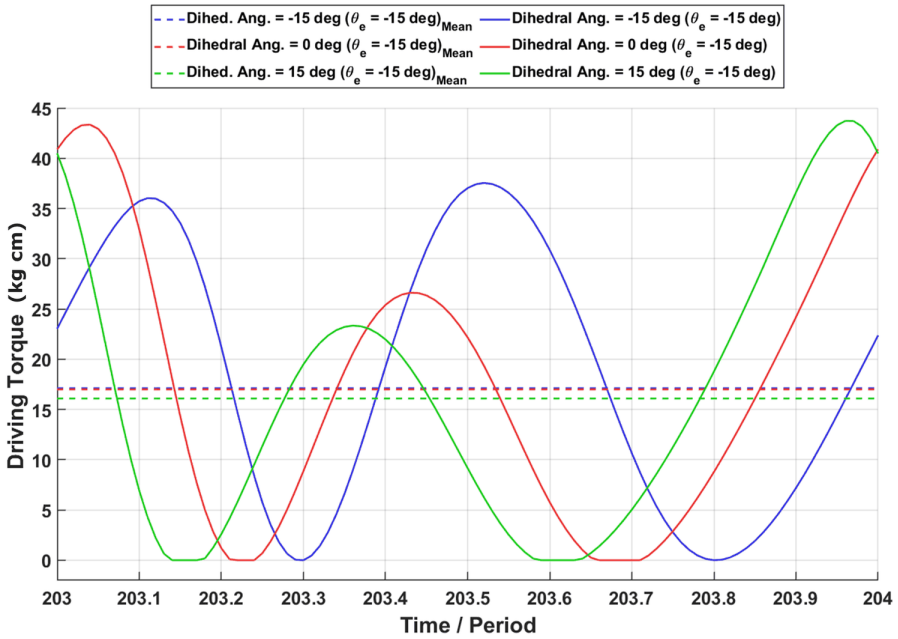


Figure 13 – Crank driving torque over one steady-state flapping cycle for the three mean dihedral angle configurations (Case B, $\theta_e = -15°$); the dashed lines denote the cycle-averaged values.

dral angle therefore improves both the longitudinal stability and the forward-flight performance while slightly reducing the mean mechanical power.

4. Conclusions

This study applied ORNISP, an integrated simulation framework that couples a modified UVLM with a multi-flexible-body dynamics model, to the aero-mechanical analysis of a single-joint bird-inspired ornithopter in forward flight. A laterally constrained forward-flight environment was constructed in which the wing kinematics are enforced over the first two flapping cycles and the longitudinal degrees of freedom are then released so that the vehicle settles into its own trim state. The framework was validated against KRoFalcon-S flight-test data over four trim conditions, predicting the trim flight speed within 3.8% and the body angle of attack within 7.8%, at a computational cost far below that of coupled computational-fluid-dynamics and computational-structural-dynamics analysis.

Forward-flight parametric studies then revealed the design trade-offs that govern the longitudinal flight dynamics. The main spar stiffness was found to control the climb capability. A spar that is too flexible (Case A) cannot generate sufficient aerodynamic force and fails to sustain flight, whereas a stiffer spar restores sustained flight. Beyond the intermediate stiffness (Case B), however, the climb rate barely increases (the trim V_z rises only from 0.2 to 0.3 m/s) while the body pitch oscillations grow and the mean mechanical power rises from 67.4 to 81.3 W. The lowest spar stiffness that meets the climb requirement is therefore the preferred design choice, with a stiffer spar reserved for missions that demand rapid altitude gain.

The mean dihedral angle was found to govern the longitudinal stability. A negative dihedral angle produced large-amplitude, phugoid-like oscillations without reaching a steady trim, whereas a positive dihedral angle of $+15°$ produced a faster, steadier flight at a lower trim angle of attack while slightly

lowering the mean mechanical power, so a positive mean dihedral angle is preferred for both stability and efficiency over the range tested. Overall, these results show that an integrated fluid-structure interaction framework can link the structural and kinematic design parameters to the resulting flight dynamics, stability, and power consumption, supporting a parametric approach to bird-inspired ornithopter design.

5. Acknowledgements

This research was supported by Unmanned Vehicles Core Technology Research and Development Program through the National Research Foundation of Korea (NRF) and Unmanned Vehicle Advanced Research Center (UVARC) funded by the Ministry of Science and ICT, the Republic of Korea (2020M3C1C1A01083415).

6. Contact Author Email Address

mailto: jaehunghan@kaist.ac.kr

7. Copyright Statement

The authors confirm that they, and/or their company or organization, hold copyright on all of the original material included in this paper. The authors also confirm that they have obtained permission, from the copyright holder of any third party material included in this paper, to publish it as part of their paper. The authors confirm that they give permission, or have obtained permission from the copyright holder of this paper, for the publication and distribution of this paper as part of the ICAS proceedings or as individual off-prints from the proceedings.

References

[1] Shyy W, Lian Y, Tang J, Viieru D and Liu H. *Aerodynamics of low Reynolds number flyers*. Cambridge University Press, 2007.

[2] Gerdes J W, Gupta S K and Wilkerson S A. A review of bird-inspired flapping wing miniature air vehicle designs. *Journal of Mechanisms and Robotics*, Vol. 4, 021003, 2012.

[3] Han J-H, Lee J-S and Kim D-K. Bio-inspired flapping UAV design: a university perspective. *Proceedings of SPIE*, Vol. 7295, 72951I, 2009.

[4] Lee S-G, Yang H-H, You H and Han J-H. Design and path following flight test of a flapping-wing air vehicle. *Proceedings of the 14th International Micro Air Vehicle Conference*, 2023.

[5] Han J-H, Han Y-J, Yang H-H, Lee S-G and Lee E-H. A review of flapping mechanisms for avian-inspired flapping-wing air vehicles. *Aerospace*, Vol. 10, 554, 2023.

[6] Nguyen A T and Han J-H. Wing flexibility effects on the flight performance of an insect-like flapping-wing micro-air vehicle. *Aerospace Science and Technology*, Vol. 79, pp 468-481, 2018.

[7] Addo-Akoto R, Yang H-H, Han J-S and Han J-H. Wing flexibility effect on aerodynamic performance of different flapping wing planforms. *Journal of Fluids and Structures*, Vol. 123, 104006, 2023.

[8] Ellington C P, van den Berg C, Willmott A P and Thomas A L R. Leading-edge vortices in insect flight. *Nature*, Vol. 384, pp 626-630, 1996.

[9] Shyy W, Aono H, Chimakurthi S K, Trizila P, Kang C-K, Cesnik C E S and Liu H. Recent progress in flapping wing aerodynamics and aeroelasticity. *Progress in Aerospace Sciences*, Vol. 46, pp 284-327, 2010.

[10] Li Q, He J, Wu C, Cui Y and Zhang B. Study on the aerodynamic characteristics of bird-like flapping wings under multi-degree-of-freedom conditions. *International Journal of Aeronautical and Space Sciences*, Vol. 26, pp 2243-2251, 2025.

[11] Liu H. Integrated modeling of insect flight: from morphology, kinematics to aerodynamics. *Journal of Computational Physics*, Vol. 228, pp 439-459, 2009.

[12] Nakata T and Liu H. A fluid-structure interaction model of insect flight with flexible wings. *Journal of Computational Physics*, Vol. 231, pp 1822-1847, 2012.

[13] Kim D-K, Lee J-S, Lee J-Y and Han J-H. An aeroelastic analysis of a flexible flapping wing using modified strip theory. *Proceedings of SPIE*, Vol. 6928, 69281O, 2008.

[14] Kim D-K, Lee J-S and Han J-H. Improved aerodynamic model for efficient analysis of flapping-wing flight. *AIAA Journal*, Vol. 49, pp 868-872, 2011.

[15] Wang Q, Goosen J F L and van Keulen F. An efficient fluid-structure interaction model for optimizing twistable flapping wings. *Journal of Fluids and Structures*, Vol. 73, pp 82-99, 2017.

[16] Katz J and Plotkin A. *Low-speed aerodynamics*. 2nd edition, Cambridge University Press, 2001.

[17] Nguyen A T, Kim J-K, Han J-S and Han J-H. Extended unsteady vortex-lattice method for insect flapping wings. *Journal of Aircraft*, Vol. 53, pp 1709-1718, 2016.

[18] Yang H-H, Lee S-G, Lee E-H and Han J-H. Numerical simulation framework of bird-inspired ornithopter in forward flight. *Journal of Fluids and Structures*, Vol. 133, 104263, 2025.

[19] Pfeiffer A T, Lee J-S, Han J-H and Baier H. Ornithopter flight simulation based on flexible multi-body dynamics. *Journal of Bionic Engineering*, Vol. 7, pp 102-111, 2010.

[20] Kim J-K and Han J-H. A multibody approach for 6-DOF flight dynamics and stability analysis of the hawkmoth Manduca sexta. *Bioinspiration & Biomimetics*, Vol. 9, 016011, 2014.

[21] Lee S-G, Yang H-H, Addo-Akoto R and Han J-H. Transition flight trajectory optimization for a flapping-wing micro air vehicle with unsteady vortex-lattice method. *Aerospace*, Vol. 9, 660, 2022.

[22] Kim J-K, Lee J-S and Han J-H. Passive longitudinal stability in ornithopter flight. *Journal of Guidance, Control, and Dynamics*, Vol. 35, pp 669-674, 2012.

[23] Ansari S A, Zbikowski R and Knowles K. Non-linear unsteady aerodynamic model for insect-like flapping wings in the hover. Part 2: implementation and validation. *Proceedings of the Institution of Mechanical Engineers, Part G: Journal of Aerospace Engineering*, Vol. 220, pp 169-186, 2006.

[24] Wie S Y, Lee S and Lee D J. Potential panel and time-marching free-wake-coupling analysis for helicopter rotor. *Journal of Aircraft*, Vol. 46, pp 1030-1041, 2009.

[25] Chace M A. Vector analysis of linkages. *Journal of Engineering for Industry*, Vol. 85, pp 289-297, 1963.

[26] Wilson C E and Sadler P J. *Kinematics and dynamics of machinery*. Pearson Education, 2003.

[27] Morton D T, Reyes A, Clausen A H and Hopperstad O S. Mechanical response of low density expanded polypropylene foams in compression and tension at different loading rates and temperatures. *Materials Today Communications*, Vol. 23, 100917, 2020.

[28] Kim S, Kim M-S, Kim S and Suk J. Design, fabrication, and flight test of articulated ornithopter. *Proceedings of the 10th International Micro Air Vehicles Conference*, 2018.

[29] FunctionBay, Inc. *RecurDyn*: multi-flexible-body dynamics simulation software. Seongnam-si, Republic of Korea. `https://functionbay.com`.

[30] Chung J and Hulbert G M. A time integration algorithm for structural dynamics with improved numerical dissipation: the generalized-α method. *Journal of Applied Mechanics*, Vol. 60, pp 371-375, 1993.